Title

Template-Enabled Biofabrication of Thick 3D Tissues with Patterned Perfusable Macrochannels

Journal

Advanced Healthcare Materials, 11(7)

ISSN

2192-2640

Authors

Davoodi, Elham
Montazerian, Hossein
Zhianmanesh, Masoud
et al.

Publication Date

2022-04-01

DOI

10.1002/adhm.202102123

Peer reviewed

HHS Public Access

Author manuscript

Adv Healthc Mater. Author manuscript; available in PMC 2023 April 01.

Published in final edited form as:

Adv Healthc Mater. 2022 April ; 11(7): e2102123. doi:10.1002/adhm.202102123.

Template-Enabled Biofabrication of Thick Three-Dimensional Tissues with Patterned Perfusable Macro-Channels

Elham Davoodi[a,b,c,d,#], **Hossein Montazerian**[b,c,d,#], **Masoud Zhianmanesh**[e], **Reza Abbasgholizadeh**[d], **Reihaneh Haghniaz**[d], **Avijit Baydia**[f], **Homeyra Pourmohammadali**[g], **Nasim Annabi**[f], **Paul S. Weiss**[b,c,h,i], **Ehsan Toyserkani**[a,*], **Ali Khademhosseini**[d,*]

[a]Multi-Scale Additive Manufacturing Laboratory, Mechanical and Mechatronics Engineering Department, University of Waterloo, 200 University Avenue West, Waterloo, ON N2L 3G1, Canada

[b]Department of Bioengineering, University of California, Los Angeles, Los Angeles, California 90095, United States

[c]California NanoSystems Institute, University of California, Los Angeles, Los Angeles, California 90095, United States

[d]Terasaki Institute for Biomedical Innovation, Los Angeles, CA 90024, United States

[e]School of Biomedical Engineering, University of Sydney, Sydney, New South Wales 2006, Australia

[f]Department of Chemical and Biomolecular Engineering, University of California, Los Angeles, Los Angeles, California 90095, United States

[g]Department of System Design Engineering, University of Waterloo, 200 University Avenue West, Waterloo, ON N2L 3G1, Canada

[h]Department of Chemistry and Biochemistry, University of California, Los Angeles, Los Angeles, California 90095, United States

[i]Department of Materials Science and Engineering, University of California, Los Angeles, Los Angeles, California 90095, United States

Abstract

Interconnected pathways in three-dimensional (3D) bioartificial organs are essential to retaining cell activity in thick functional 3D tissues. Three-dimensional bioprinting methods have been

[*]Corresponding Authors: Ali Khademhosseini, khademh@terasaki.org; Ehsan Toyserkani, ehsan.toyserkani@uwaterloo.edu.
[#]E.D. and H.M. contributed equally to this work.

Author Contributions

ED and HM equally contributed to this work. The idea was developed, outlined, and most of the experiments were performed, analyzed, and reported by HM and ED. MZ conducted CFD analysis of scaffolds. RA and RH analyzed the *in vivo* data. RH assisted HM and ED in degradation studies and biocompatibility assays. HA, NA, and PSW provided insightful comments and contributed to the methodology. The work was supervised by ET and AK. ET and AK also contributed to analyses of the data and writing of the manuscript.

The authors declare no competing financial interest.

Supporting Information

Supporting Information is available from the Wiley Online Library or from the author.

widely explored in biofabrication of functionally patterned tissues; however, these methods are costly and confined to thin tissue layers due to poor control of low-viscosity bioinks. Here, cell-laden hydrogels that could be precisely patterned *via* water-soluble gelatin templates are constructed by economical extrusion 3D printed plastic templates. Tortuous co-continuous plastic networks, designed based on triply periodic minimal surfaces (TPMS), served as a sacrificial pattern to shape the secondary sacrificial gelatin templates. These templates were eventually used to form cell-encapsulated gelatin methacryloyl (GelMA) hydrogel scaffolds patterned with the complex interconnected pathways. The proposed fabrication process was compatible with photo-crosslinkable hydrogels wherein prepolymer casting enabled incorporation of high cell populations with high viability. The cell-laden hydrogel constructs were characterized by robust mechanical behavior. *In vivo* studies demonstrated a superior cell ingrowth into the highly permeable constructs. Perfusable complex interconnected networks within cell-encapsulated hydrogels may assist in engineering thick and functional tissue constructs through the permeable internal channels for efficient cellular activities *in vivo*.

Graphical Abstract

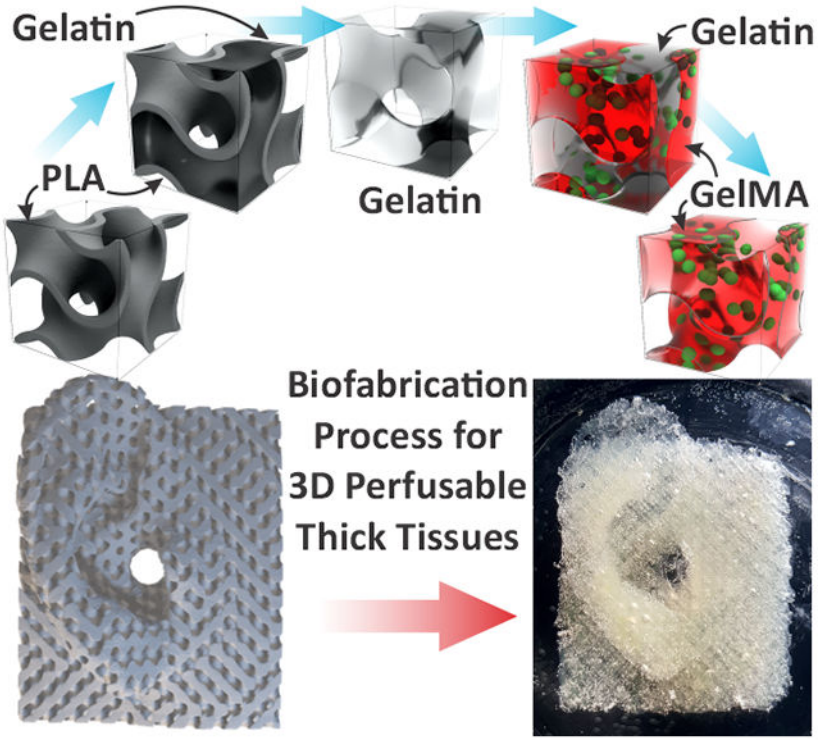

A biocompatible, economic, and robust biofabrication process was developed to form complex shapes and internal perfusable channels in multilayered thick tissue constructs made from extracellular matrix mimicking soft hydrogels (*i.e.*, gelatin methacryloyl, GelMA). Cell-laden GelMA hydrogels with interconnected pores demonstrated excellent mechanical tunability and supported cell function *in vitro* and *in vivo*.

Keywords

biofabrication; 3D bioprinting; cell-laden hydrogel; gelatin methacryloyl; additive manufacturing

1. Introduction

Continuous delivery of nutrients and removal of waste products are essential functions for the survival of bulky multi-cellular tissues and promoting the metabolic activities of living organs.[1] Blood vessels, as interconnected pathways, can facilitate such delivery by the circulatory system to many tissues. Engineering synthetic multi-cellular and functional tissues requires a comprehensive network of interconnected channel pathways to enable the distribution of metabolites.[2] Tremendous efforts have been made to recapitulate the vasculature networks in native organs; however, state-of-the-art techniques nonetheless fail to fabricate scalable and robust vascularized tissue constructs.

Multiple approaches have been explored to develop three-dimensional (3D) complex tissues engineered with incorporated internal pores/channels. Conventional techniques such as gas foaming,[3] freeze-drying,[4] and particulate leaching[5] have proven to be less appropriate for biofabrication of functional tissues, due to their limited pore interconnectivity and/or insufficient control on the pore shape. Three-dimensional bioprinting, which is layer-by-layer assembly of bioinks,[6] has shifted the focus of biofabrication interests within the last few decades. Extrusion-based 3D bioprinting (also known as bio-additive manufacturing),[7] material-jetting,[8] digital light processing,[9] and stereolithography[10] have been widely reported. Despite many advantages offered by extrusion 3D bioprinting, they have been accompanied by drawbacks such as nozzle clogging and limited resolution.[11] The low viscosity of most bioinks, which are often difficult to handle, and the demand for layer-by-layer curing impose other challenges such as control over the physical properties of the bioinks and structural integrity of the final 3D bioprinted tissue constructs.[12] In these methods, increasing the cell density beyond a certain limit results in nozzle clogging, and thereby the augmented shear forces transferred to the cells from the bioink flow can cause cell death.[13] In addition, cell sedimentation during the 3D bioprinting process has been a major issue, leading to heterogeneous cell distributions in the final constructs.[14]

Template-based biofabrication approaches can enable engineering 3D constructs from soft hydrogels that are often challenging to be directly 3D bioprinted. In this approach, a 3D printed sacrificial template is embedded into a soft hydrogel that is cured later after the casting process.[15] This step is followed by sacrificing the template to reveal the resulting hydrogel with an internal 3D interconnected network of open channels inscribed by the original interconnected templates. Nozzle injection in the conventional 3D bioprinting methods is replaced with casting processes to facilitate loading larger populations of cells and eliminate shear-force-induced cell death as well as cell sedimentation. The sacrificial templates must be transparent to prevent shadow artifacts that would hinder the curing process for the infilled hydrogel matrices with ultraviolet (UV) or visible light-based crosslinking mechanisms.[2b, 16] Bio-templating also requires sacrificial templates that can be safely washed away. Three-dimensionally printed sacrificial templates from a

multitude of candidate materials such as gelatin,[17] pluronic,[2a, 2c, 18] poly(vinyl alcohol),[19] alginate,[20] and carbohydrate mixtures[2b, 16, 21] have been demonstrated in the literature, each of which, however, has its own limitations. For instance, carbohydrate-based templates[2b] were fabricated by hot melt extrusion-based 3D printing;[2b] however, the 3D printed constructs were mostly restricted to few-layer lattice-shaped patterns due to difficulties in controlling the ink physical properties and its deposition in multi-layered constructs. Therefore, the ink characteristics needed to be tuned *via* mixing with other additives such as dextran, sucrose, and glucose, which requires further practice and burdensome optimization processes.[2b] In another example, a mixture of isomalt powder and cornstarch was used for fabricating vasculature templates, using a selective laser sintering (SLS) platform. Selective laser sintering may face challenges in the depowdering stage when it comes to bulky constructs with fine porous architectures. The opaque optical properties of the templates can present another obstacle to the later prepolymer photopolymerization to obtain 3D thick constructs. Gelatin, a thermo-responsive (liquid at 37 °C and forms gel at the room temperature) and water-soluble candidate, could be more favorable as sacrificial material in template-based biofabrication, due to its cell friendly nature. However, direct extrusion printing of gelatin could be highly challenging due to its low viscosity and slow physical gelation with temperature, leading to structural self-collapse, especially for printing overhanging features. This matter limits the resolution, complexity, and precision of the final constructs and therefore only works for printing patterned 2D structures.[16]

Leveraging our previous experience in developing silicone constructs through template-assisted techniques,[22] we propose a robust, accessible, and economical double-templating fabrication process to develop gelatin sacrificial templates with complex and fine internal features. Gelatin molds serve to fabricate 3D thick cell-laden hydrogels with interconnected macro-channels. In this process, we aim to construct gelatin methacryloyl (GelMA) structures from low viscous cell-laden prepolymers, which are often difficult to process using the extrusion 3D bioprinting methods. The superior control on the internal channel architectures is demonstrated in porous hydrogels designed based on tortuous triply periodic minimal surfaces (TPMS), known as P and D structures. Design parameters in these scaffolds were also employed to tune the mechanical and biopermeability properties. Finally, the *in vitro* and *in vivo* studies are conducted to demonstrate bioactivity of the engineered GelMA constructs for fabrication of functional tissue replacements.

2. Results and Discussion

2.1 Template-based fabrication of tissue constructs

The fabrication scheme for the development of internally channeled soft tissue constructs is illustrated in Figure 1a. First, poly(lactic acid) (PLA) primary molds designed based on TPMS architectures (Figure S1) were fabricated *via* the fused deposition modeling (FDM) technique (Figure 1aI and Figure S2I). The FDM-based extrusion 3D printing techniques are well established and accessible with the lowest cost among 3D printing techniques. The bulky 3D tortuous features of porous TPMS architectures can be 3D printed, often with no need for support materials. Dissolving FDM 3D printed plastic templates, however, requires

harsh solvents that could damage living cells. Hence, the PLA templates were cast with gelatin to enable the precise fabrication of water-soluble gelatin secondary templates. Note that we initially considered water-soluble carbohydrate secondary templates such as isomalt. However, molten isomalt (at ~130 °C) tends to quickly solidify while casting in the PLA template, hindering full penetration into the pores. Hence, we found it challenging to form carbohydrate templates as higher temperatures could also thermally distort the 3D printed plastic PLA template.

Gelatin solution (10 %w/v) at higher temperatures (~80 °C, well below the melting temperature of PLA, *i.e.*, 150-160 °C) was liquid enough to infuse fully within the channels of the PLA template with the aid of vacuum. Cooling the gelatin infilled PLA template down to ~4 °C led to the *in situ* physical gelation of gelatin. This step was followed by dichloromethane (DCM) treatment that led to the successful removal of PLA, leaving behind the porous gelatin construct to which the PLA pattern was fully transferred (see Figure 1aII and Figure S2II,III). Note that we initially used acrylonitrile butadiene styrene (ABS) and acetone as a primary sacrificial template and the solvent in our gelatin template fabrication system (for dissolving ABS), respectively; however, the gelatin was distorted upon immersion in acetone (see Figure S3), whereas no visible shape changes were observed in the case of DCM. In addition, DCM is highly volatile and hardly miscible with water, thereby it could be easily removed from gelatin when immersed in aqueous media, as illustrated in Figure 1aIII and Figure S2III. In essence, a thin film of DCM, which can easily evaporate, was observed on the surface of the water bath after soaking the DCM-treated gelatin template.[23] Part of the DCM, as it replaces with water, sank into the water bath per the higher density of DCM that facilitates its removal from the gelatin template. The removal of DCM from gelatin was further confirmed by gas chromatography mass spectrometry (GCMS). The results shown in Figure S4 indicate that the peak at 2.17 min (corresponding to DCM) did not appear in both gelatin templates dialyzed in freshwater bath as well as final GelMA constructs suggesting successful removal of DCM (accuracy within ~5 ppm range).

Visible light crosslinkable cell-laden GelMA prepolymer was pipetted into the gelatin templates followed by a photo-crosslinking process. Due to the hydrophilicity of both GelMA and gelatin,[24] and co-continuous phases of the templates, the gelatin template was fully filled upon casting GelMA prepolymer with no observable evidence of bubble formation (Figure 1aIV and Figure S2IV). Irradiating the GelMA prepolymer (containing Eosin Y as a photoinitiator, triethanolamine (TEA) as co-initiator, and *N*-vinylcaprolactam (VC) as co-monomer) with visible light resulted in a color change from red to yellow as shown in Figure S2V, which was indicative of crosslinking reaction. Visible light was irradiated until a uniform color change was obtained across the structure, to minimize crosslinking gradients. The use of visible light crosslinking in this approach is expected to pose a lower risk of cell damage compared to the ultraviolet (UV)-light-initiated polymerization.[25] The gelatin template was fully dissolved in the cell-culture media during the incubation at 37 °C (or in warm water for the cell-free experiments), leaving behind the 3D self-standing porous GelMA construct shaped in accordance with the primary PLA template (see Figure 1aV,b and Figure S2VI).

The proposed fabrication process enabled the successful transfer of the designed patterns to the cell-laden GelMA hydrogels and allowed multiple layered constructs with complex channel shapes at thickness levels significantly larger than those demonstrated in the literature.[26] The proof-of-concept scaffolds with ~1 cm thickness and ~2 cm diameter with micro-scale pore features corresponded well to the original topology of 3D printed PLA templates. We could also successfully fabricate complex human tissue models with overhanging features (*i.e.*, ear and nose) with tortuous internal pore shapes (D structure) as represented in Figure 1c,d and Figure S5. To assess pore interconnection within those structures, the nose model was freeze-dried and micro-computed tomography (μ-CT) images were taken (Figure 1dI,II). The pore patterns of D structure could be seen across the cross-sections. The fabrication process was also able to form open channels with blood vessel shapes allowing robust fluid flow (Figure 1(e)). Overall, in this method, since the main geometry originates from the FDM 3D printing technology, the pores with high precision are compared favorably to what direct extrusion 3D bioprinting technologies could achieve. Although extrusion bioprinted constructs in the literature are typically limited to thin layer constructs (due to difficult prepolymer handling of low-viscosity bioinks), template-based fabrication can form highly complex geometrical features in thick structures at the similar prepolymer concentrations.[27] Therefore, as opposed to extrusion bioprinting techniques, which require shear-thinning bioinks, the proposed technique enables bioprinting of low-viscosity Newtonian solutions. Although multiple steps are required here, which is less of concern when it comes to personalized medicine, the low cost and accessibility of instrumentation can benefit a larger population of patients. The presented fabrication process offers flexibility in terms of the encapsulated cell population due to the elimination of nozzle clogging issues. This method can be easily tuned to form a wide range of cell-encapsulated hydrogels with desirable architectures.

2.2 Optimization of the fabrication process for printing fidelity

The first stage of the fabrication process, *i.e.*, 3D printing of PLA template, determines the basic topology of the final GelMA constructs. Hence, in our initial attempt, we strived to find the smallest TPMS unit cell sizes where (i) the FDM 3D printer could properly fabricate the samples and (ii) gelatin could fully infill the templates without leaking into the hollow PLA mold. The most challenging geometry in our experience (*i.e.*, the D pore shape at 0.70 relative density (RD) due to its topological tortuosity and small room for gelatin diffusion) was 3D printed at different unit cell sizes, as represented in Figure 2a, and inspected for defects. The results showed that at the unit cell sizes above ~3.3 mm, the pores could be successfully formed as in their corresponding CAD models, whereas the scaffolds with smaller unit cell sizes had notable defects, and the pores were not coherently formed. Accordingly, the gelatin negative image of the PLA template was formed with no evident flaws or defects (Figure 2b), suggesting complete infusion of the gelatin into the PLA pores. At this scale, the sub-millimeter size features (pore sizes and connections) starting from ~800 μm were measured in both PLA and gelatin constructs. Moreover, the stair-step topology of the PLA surface because of the layer-by-layer 3D printing was clearly transferred onto the gelatin template in micro-scale.

In the next step, the physical properties of the secondary gelatin templates were assessed as shown in Figure 2c–e. Gelatin in the first place was required to be self-standing and firm enough to support the casting material. We examined gelatin contents over the range of 5, 10, 15, and 20 %w/v for the fabrication of P structures at 0.42 gelatin RD. Gelatin templates at 5 %w/v tended to collapse as they failed to withstand their own weight and thereby could lead the final GelMA scaffold to deviate structurally from their designed models. The swelling behavior of gelatin in water during the DCM removal could be another aspect of topological deviation, as investigated in Figure 2c–e. The volumetric swelling ratio decreased from ~37% to ~14% as the gelatin concentration reduced from 20 %w/v to 10 %w/v (Figure 2d). This difference is because the lower dry gelatin content was less capable of absorbing fluids.[28] Thus, the lowest gelatin concentration of 10 %w/v was chosen in our fabrication process as it minimized gelatin swelling while maintaining the required structural integrity. In the context of pore size, the swelling behavior can have a competing effect: water uptake in gelatin templates simultaneously caused an overall expansion, while thickening the internal linkages and connections locally reduced the pore size. Apart from the minimal volumetric swelling, the low gelatin content facilitated gelatin removal from the GelMA network in the later stages of the fabrication process. We investigated the effect of gelatin RD on the volumetric swelling behavior. The results of swelling across different RD values for the P structure suggested an overall increase in gelatin swelling with RD, where the maximum volumetric swelling remained within ~28% at the maximum RD.

Next, we sought to engineer self-standing patterned GelMA hydrogels, yet with minimized prepolymer concentration, in order to provide a more favorable extracellular matrix (ECM) for cell encapsulation and media diffusion. We noted that the initiation mechanism for the polymerization of GelMA played a key role in our fabrication process to form crosslinked GelMA networks in the gelatin templates (Figure 2f). For instance, we initially attempted to crosslink a 10 %w/v GelMA prepolymer using a 0.5 %w/v Irgacure 2959 photoinitiator solution under UV light (25 mW/cm^2) for 2 min. However, GelMA failed to fully crosslink as it completely dissociated in warm water during the gelatin removal process (Figure 2fI). Therefore, a redox ammonium persulfate (APS)/*N,N,N,N*-tetramethylethylenediamine (TEMED) initiator system, which is widely used for free-radical polymerization in hydrogels, was used at different 1:1 compositions to crosslink 10 %w/v GelMA prepolymers. A GelMA prepolymer solution containing 0.3 %w/v of APS and 0.4 %w/v of TEMED was left at room temperature overnight for the crosslinking reaction. The resulting hydrogel had poor mechanical stability, containing partially crosslinked hydrogel clumps (Figure 2fII). On the other hand, increasing the APS and TEMED concentrations to 0.5 %w/v led to the rapid gelation of GelMA and thereby failed to completely fill the gelatin templates. The observed failures in crosslinking can be explained by either limited penetration length of light or possible initiator dilution driven by the diffusion of small initiator molecules into the gelatin phase. Switching over to the EosinY/VC/TEA visible light-triggered initiation system, however, enabled the successful fabrication of 10 %w/v GelMA constructs with the designed internal pore architectures (Figure 2fIII). The use of visible light is highly preferred over UV light due to biosafety. Note that lowering the GelMA concentration to 5 %w/v failed, as the structure was not strong enough to withstand its own weight and thereby collapsed after the gelatin removal process (although it retained

its shape when immersed in water). Therefore, we selected the 10 %w/v GelMA as the lowest concentration for hydrogel formation for the remaining characterizations.

The fabrication process was implemented on a variety of pore shapes (*i.e.*, P and D pore shapes) and RD values (*i.e.*, 0.30, 0.42, 0.58, 0.70) to test the versatility of the proposed process for engineering complex 3D GelMA constructs. The optical microscopic images of the PLA and gelatin templates, as well as GelMA scaffolds in various pore shapes and relative densities, are presented in Figure S1. The overall RD of the final constructs was obtained by dry weighing and compared with the designed CAD models in Table S1. The results suggest that the RD for the as-fabricated samples deviated within ~17% from the designed CAD model. Figure 2gI demonstrates the pore size and topology of connections in swollen P structure at different RD values. As can be seen, the pore/channel sizes in the range of ~0.9 mm to ~2.2 mm could be fabricated in a controllable manner. The measured pore sizes were also found to be in agreement with those of CAD models (Table S1). The stair-step surface topology on gelatin molds (Figure 2bII) was also transferred to the final GelMA scaffolds (Figure 2gII).

2.3. Swelling, degradation, and drug release responses

The physical properties of the GelMA constructs fabricated with the P structure at different RD values were characterized in terms of their swelling, degradation, and drug release performance in response to exposure to biofluids (see Figure 2h–j). The scaffolds had swelling ratios in the range of ~24% to ~40% for various RD values (Figure 2h). The swelling ratio of the scaffolds was not significantly correlated with the RD. The enzymatic degradation of the GelMA scaffolds with a 10 μg/ml collagenase solution showed accelerated degradation rates for the samples with larger RD (Figure 2i). This observation is in agreement with the previously reported data.[29] In addition, porous GelMA constructs were evaluated in terms of their drug release performance. To load drug molecules, the GelMA scaffolds were soaked for 4 h in a 30 mg/L Rhodamine B solution, as a model molecule representative of small-molecule drugs such as those with antimicrobial functions. The release of Rhodamine B was obtained over time for scaffolds with different RD. Overall, the lower the RD, the faster the release kinetics due to the thinner internal features and thereby easier transfusion of the drug molecules.

2.4 Quasi-static compressive mechanical behavior

The mechanical properties of the scaffolds were evaluated under quasi-static monotonic compressive deformations. The effect of GelMA concentration on the compressive response of the P scaffolds at 0.42 RD is shown in Figure 3a. The compressive stress-strain curves of the GelMA scaffolds were in line with soft porous materials.[30] The stress-strain curves initiated with a linear elastic region followed by sharp increases in stress, corresponding to collapse of the internal layers. Then, densification was observed while compaction of the polymer chains and failure progressed. Elastic modulus was increased by ~250% as the GelMA concentration raised from 10 to 20 %w/v (Figure 3b). The systematic failure in scaffolds was originated from the brittle failure of the connections in the internal scaffold structure (Figure 3c).

Deformation and failure mechanisms of the scaffolds are critical in determining the mechanical behavior of scaffolds. Figure 3d illustrates the mechanism of structural instabilities in different pore shapes and RD levels. Deformation and failure in porous biomaterials are often classified with respect to the pore shape as stretching (P structure) and bending (D structure) dominated mechanisms. The compressive deformation of the P structure strongly depended on the scaffold RD. At low RD, *i.e.*, 0.30, axial deformation was transferred to buckling of the vertical connections (Figure 3dI), whereas, at 0.70 RD, most elements were subject to axial compression (Figure 3dII). For the D structure, compression loads were transferred to shear deformation across the RD values (Figure 3dIII). The stress-strain curves for the porous GelMA scaffolds are shown in Figure 3e. The linear elastic region continued up to the strains of ~0.4 for most samples before the first failure was observed. The brittle failure of internal linkages corresponded to sharp drops in stress-strain curves. This result is in accord with a layer-by-layer failure mechanism in both P and D surface topologies. As shown in the magnified plot insets in Figure 3e, while P structures showed failure at compressive strains below 0.4, D structures showed rather smooth behavior. As shown in Figure 3f, the elastic modulus of the scaffolds increased with RD. The elastic modulus was in the range of 2.8-12.5 kPa and 1.6-6.5 kPa for P and D structures, respectively. The observed range of elastic moduli matches those of soft tissues such as skeletal muscle tissue, smooth muscle tissue, as well as arteries.[31] The larger elastic moduli for P structures can be due to the stretching-dominated deformation mechanism. The results of scaling analysis (power fit) to the elastic modulus-RD data are represented in Table S2. The exponential constants of 1.64 and 1.53 were obtained for P and D structures, respectively, which are comparable to previously reported results.[30]

2.5 Cyclic Compression test on GelMA scaffolds

Tissue constructs are often subject to dynamic deformations. Hence, the compressive stress-strain properties of the GelMA scaffolds were evaluated under cyclic loads with increasing strain magnitudes from 0.05 to 0.50 (see Figure 3g). A wide hysteresis region and stress-strain shift with increasing loading cycles are indicative of plastic and irreversible deformations. As shown in Figure 3e, the hysteresis curves indicated reversible deformations with minimal energy loss at the strain amplitudes below their corresponding failure strain. For instance, the evidence of large hysteresis was more prominent in P structures at higher RD values of 0.58 and 0.70 (and D structure at 0.70 RD) as the curves tend to shift with increasing deformation amplitudes beyond its failure point. The hysteresis ratio, as an indicator of permanent deformations and dissipated deformation energy under dynamic loading, was quantified in Figure 3h. Hysteresis ratio varied in the same range of ~0.10 to ~0.65 within the applied deformation range for both P and D structures and increased with both strain amplitude and RD. In general, a reversible elastic behavior was maintained in D structures at higher RD than P structures. This result is consistent with postponed failures in quasi-static loading data (Figure 3e) for D structures and could be due to the capability of bending-dominated structures in reversible deformation energy absorption. The larger hysteresis cycles in P structures indicated buckling/axial deformation-induced permanent failures.

2.6 Permeability analysis of hydrogel scaffolds

Permeability measurement is a quantitative approach representing the capability of the scaffolds to transfer nutrients and body fluids. Here, the effect of pore shape and RD on the permeability of the scaffolds was assessed *via* a constant head permeability test (Figure 4a). The fluid flow, measured at various fluid heights (15-45 mm), showed a linear relation between pressure (P) and flow rate (Q) for all scaffolds (Figure 4b). The higher slope of the P-Q plots observed for the scaffolds with higher RD signifies the lower fluid permeability based on Darcy's law.[32] As the fluid height increased, the permeability decreased for the scaffolds with lower RD values, potentially due to the deviations from the laminar flow and pressure head loss (Figure S6). The permeability of the scaffolds was obtained by using a linear fit to the P-Q curve; the calculated permeability values are shown in Figure 4c. The permeability of the scaffolds varied inversely with RD values from 1.34×10^{-10} to 9.18×10^{-10} m^2. The experimental permeability was exponentially correlated to the RD according to the results of the fit to data presented in Table S2. The fluid flow was computationally analyzed, and corresponding computational permeability values were calculated using computational fluid dynamics (CFD). Figure S7a presents the computational permeability data. The larger permeability for the P structure at lower RD values was reflected in the experimental data and can be explained by the predicted fluid flow streamlines. Figure 4d illustrates the 3D fluid flow patterns along a linear path at the scaffold inlet for P and D structures (0.42 RD). The full 3D and 2D (top view) demonstration of the fluid flow is shown in Figure S8 and Figure S9, respectively. The fluid flow for the P structure mostly fell onto a 2D plane and followed more direct pathways compared to the D structure, whereas the flow in D scaffolds followed a swirling path due to the tortuous nature of the unit cell topology in the internal scaffold structure. At high RD values, this trend switched due to the inhomogeneous distribution of channel width in the P structure. Note that surface area for TPMS scaffolds studied here are maximum at RD ~0.5.[33]

2.7 *In vitro* and *in vivo* Biocompatibility

To assess the biosafety of the proposed fabrication process and the GelMA porous constructs for potential use as tissue substitutes, *in vitro* cell compatibility of the cell-laden constructs was evaluated by using a live/dead assay. For this purpose, the cell-encapsulated GelMA scaffolds (P-surface at 0.58 RD) and GelMA sheets as control (~1 mm thickness) were prepared and evaluated in terms of cell viability for a period of 5 days. Representative live/dead fluorescent images of cell-laden scaffolds for days 1, 3, and 5 are presented in Figure 5a. For both sheet-like and porous GelMA samples, the 3T3 fibroblast cells (10 million cells/ml) remained alive (shown in green) and a few dead cells (shown in red) were seen. The live/dead assay suggested cell viability of larger than 90% throughout the course of the experiments (Figure 5b). This result indicated that the final gelatin templates were free of toxic residues (*e.g.,* DCM) and was consistent with the biocompatibility of the proposed fabrication process. The interconnected macropores formed in the hydrogel matrix enabled continuous perfusion of nutrients and maintaining high cell viability in thick scaffolds (Figure 5c). The fluorescent images captured from different sections of the porous GelMA scaffolds confirmed the viability of cells in all regions (Figure S10). The scaffolds (P structure) at different RD of 0.42 and 0.58 were implanted *in vivo* and the samples were

analyzed by hematoxylin and eosin (H&E) stain staining after two weeks of implantation. As it can be seen, as opposed to bulk GelMA controls, the highly porous scaffold of P0.42, which was characterized with high permeability and pore size, allowed cell ingrowth inside the hydrogel structure. A larger number of cells within the hydrogel material in P0.42 compared to P0.58 was also evident. This observation emphasizes the role of permeable pores within the tissue models for successful integration with the surrounding tissue. Cell adhesive GelMA scaffolds can be used to seed cells onto their surface in dynamic culture systems.

3. Conclusions and Prospects

Direct 3D bioprinting methods have been constrained to thin tissue constructs with simple shape and low cell populations. In this study, we demonstrate a bio-templating fabrication scheme to enable biofabrication of 3D thick micro-engineered tissue with better versatility to incorporate complex-shaped interconnects inside the construct compared to the direct extrusion bio 3D printing techniques. The proposed fabrication method employed accessible and low-cost materials and 3D printing instruments to provide an easy-to-access tissue fabrication platform. Using the proposed fabrication technique, highly biocompatible cell-laden GelMA hydrogel scaffolds with tunable designs of perfusable networks and tortuous complex pathways for the desired mechanical and fluid transport properties were successfully fabricated. The complex design with tortuous interconnected macropores maximizes the scaffold surface area, enabling effective diffusion of nutrients through the hydrogel matrix for uniform cell proliferation. The cell-encapsulated hydrogels showed high cell viabilities (~90%) that corroborated the biocompatibility of the process. The fabrication strategy is designed to be compatible with low viscosity hydrogels that are difficult to 3D-print. The possibility of visible light-activated crosslinking mechanisms provided a safe means of incorporating living cells with large populations inside the scaffold matrix. The hydrogels can be encapsulated with the different types of mammalian cells at physiologic density values mimicking human tissues for long-term sustainability. The proposed fabrication process is a versatile tool for developing bulky tissues from a multitude of polymer backbones. The facile and cost-efficient nature of the proposed fabrication procedure can provide a transformative platform for a wide range of tissue engineering applications and can be scaled up to form thick tissue constructs. Further development can adapt template-based 3D bioprinting to multi-material systems with directional material gradients through stepwise casting and crosslinking for applications such as regeneration of hard-to-soft tissue gradients.

4. Experimental Section

Design of triply periodic minimal surface (TPMS) sacrificial templates:

The PLA sacrificial templates were designed based on triply periodic minimal surfaces (TPMS). TPMS topologies are defined by the following general formula (Equation (1)):[30]

$$\varphi(\mathrm{r}) = \sum_{l=1}^{L} \sum_{m=1}^{M} \mu_{lm} \cos(2\pi \kappa_l (P_m^T \cdot r) = C \quad (1)$$

where μ_{lm} is the periodic moment, κ_l indicates the scale parameter, and $P_m = [a_m,\ b_m,\ c_m]^T$ and $r = [x,\ y, z]^T$ are the basis vector and the location vector in 3D space, respectively. The topology of the TPMS is governed by the left-hand side of Equation (1) and the RD is defined by the C value. Here, $\varphi < C$ represents the domain that is embraced by the TPMS topology, and $\varphi > C$ indicates the negative phase. In this study, since two sacrificial templates are used, the final GelMA scaffold mimics the shape of the initial sacrificial template. Hence, PLA templates were designed by defining $\varphi < C$. The designed models in the present paper involve P and D structures at RD values of 0.30, 0.42, 0.58, and 0.70. The corresponding offset values and explicit functions defined to obtain the models were explained elsewhere.[30] To produce the stereolithography (STL) models for 3D printing, black and white cross-sectional images of each scaffold were generated using MATLAB code (available at https://github.com/hmontazerian/TPMSCross-sectionalImageCreator.git) and imported into an image processing software (FIJI) to stitch as an STL file. Then, the cylindrical scaffolds with a unit cell size of 3.33 mm shaped with P-surface and D-surface pore shapes at the uniform RD values of 0.30, 0.42, 0.58, and 0.70 were generated. A cylindrical shell-like wall (with an outer diameter of 23.2 mm, height of 25 mm, and thickness of 0.6 mm) was also added to the STL design to perform as a reservoir to guide liquid gelatin into the PLA templates

Three-dimensional (3D) printing of sacrificial templates:

GrabCAD (GrabCAD Inc., Massachusetts, USA) software was used to import the models and define the printing parameters and tool paths. The 3D printing process was performed using a material extrusion (*i.e.,* FDM) system (LulzBot TAZ, Colorado, USA) for 3D printing of the PLA templates (first sacrificial template). The PLA filament was fed into the 3D printer and layer height was set to 0.1 mm. The nozzle and bed temperature were set to 210 °C and 60 °C, respectively. Poly(lactic acid) templates with P- and D-surface pore shapes at uniform RD values (including 0.30, 0.42, 0.58, and 0.70) were 3D printed. No extra supporting material was used for 3D printing the PLA templates. To fabricate the second sacrificial templates, the gelatin from porcine skin was dissolved in deionized water (10 %w/v) at 80 °C, and cast into the PLA templates when heating at 80 °C and under vacuum conditions. Then, the PLA/gelatin structures were cooled down to 4 °C to solidify the gelatin phase. Then, the construct was immersed in 200 ml dichloromethane (DCM) for 12 h (stirring at ~120 rpm) at room temperature to dissolve the PLA templates. The dichloromethane was refreshed two times during the dissolution process. The samples were washed with DCM to remove PLA residues and then kept in DI water overnight to remove the DCM from gelatin. For the cell-encapsulated samples, the gelatin templates were sterilized under UV for approximately 30 min for cell studies.

Fabrication of porous hydrogels:

The gelatin methacryloyl (GelMA) hydrogel was cast in gelatin templates to fabricate the porous hydrogel scaffolds. A visible light crosslinking method was employed based on a published protocol.[34] Briefly, a 10 %w/v GelMA solution, containing 6.92×10^{-3} %w/v Eosin Y as a visible light photoinitiator, 1.33 %v/v of triethanolamine (TEA) as a co-initiator, and 1 %w/v of *N*-vinylcaprolactam (VC) as a co-monomer, was prepared

in phosphate-buffered saline (PBS) for cell-free experiments and medium followed by filtration for cell studies. To encapsulate cells for cell studies, 3T3 cells were suspended in GelMA solution and infilled within the gelatin templates (at 10 million cells/ml). The cell-encapsulated GelMA was cured by exposing visible light (~100 mW/cm^2 intensity) at 450–550 nm wavelength for ~8 min using a Genzyme FocalSeal LS1000 Xenon Light.

The cell-encapsulated GelMA/gelatin samples were left in a 75 cm^2 cell culture flask with 10 ml fresh Dulbecco's Modified Eagle Medium (DMEM) media and placed on a shaker (at ~110 rpm) in a Thermo Forma, Thermo Fisher Scientific incubator set at 37 °C to allow gelatin template to dissolve overnight and make porous cell-encapsulated GelMA scaffolds. For the studies where no cells were involved, the gelatin was removed by soaking and agitating the construct in warm (~60 °C) water for ~1 min, and the GelMA prepolymer solution was prepared in DI water.

Structural characterization:

Scanning electron microscopy (SEM) imaging was performed to characterize the microscale features on the surface of the scaffolds. For this purpose, a 10 nm layer of gold was sputtered on the sample surfaces. Imaging was then performed at 20 kV using a 1550 FESEM, Zeiss, Oberkochen, Germany instrument. The internal architecture of the porous human models in freeze-dried GelMA samples was assessed using a micro-computed tomography (μ-CT) scanner (Xradia 520 Versa, Zeiss, Germany) at 40 kV voltage, and 50 μm voxel size. The imaging data was post-processed using Dragonfly software.

Gas chromatography mass spectrometry:

Gelatin templates after washing in 5 L water containers (at 4 °C overnight), as well as the final GelMA scaffolds, were examined for DCM residues. The gas chromatography mass spectrometry (GCMS) measurements were carried out using an Agilent 6890N GC, 5975 MSD, and 7683B Autosampler. Enhanced Chemstation software version E.01 was used to control the instrument and collect the data. The gas chromatography (GC) inlet was operated in split mode at 250 °C. A carrier gas, UHP He (Airgas West, Culver City, CA) with a flow rate of 1.2 ml/min was used. Separation was performed on a 30 m × 250 μm × 0.25 μm HP5-MS column obtained from Agilent J&W. The GC oven was initially held at 80 °C, heated to 130 °C at 10 °C/min, and then to 250 °C at a rate of 30 °C/min. The MSD was operated in the scan mode and electron ionization was used. Instrument response for known concentrations of pure DCM in water was measured to determine the analyte concentrations in the samples.

Swelling and degradation:

To measure the mass swelling ratio, porous GelMA scaffolds were weighed as fabricated. Then, the samples were incubated in PBS at a 37 °C incubator. The mass values were recorded at various time points, and the swelling ratios were obtained accordingly.

To assess the degradation behavior of the scaffolds, the samples were washed with PBS and freeze-dried for 3 days using a benchtop freeze drier (Labconco, MO, US). The initial dry weight was recorded as W_0. Subsequently, the dry samples were placed in a 12-well tissue

culture plate and immersed in 4 ml of freshly prepared collagenase (10 μg/ml) followed by incubation at 37 °C for pre-determined time points. At different time points, samples were removed, thoroughly washed with PBS, blotted using a Kimwipe, and freeze-dried before measuring their weight (W_d). The percent degradation rate (DR) was calculated using Equation (2):

$$\mathrm{DR}(\%) = (W_0 - W_d) \times 100 / W_0 \quad (2)$$

The collagenase enzyme was replaced every 2 days to maintain the enzyme activity. All the measurements were repeated for four samples.

Mechanical characterization:

To assess the mechanical properties of as fabricated scaffolds, monotonic and cyclic compressive tests were conducted using a mechanical testing system (Instron 5943, USA) equipped with a 100 N load cell. To prevent sliding the GelMA scaffolds, the grippers were covered with a sheet of coarse tissue paper. The monotonic compressive load was performed at crosshead displacement of 90% at 2 mm/min displacement rate. The cyclic tests were conducted in an increasing strain amplitude for each cycle (including 5, 10, 15, 20, 30, 40, and 50%) at the rate of 5 mm/min. Hysteresis was defined as $h = \frac{R_{unloading} - R_{loading}}{R_{loading}}$, where R illustrates the area under the stress-strain curves.

Permeability test:

A constant head experimental setup was employed for measuring permeability of the scaffolds. Initially, the scaffold was fit in a hole at the bottom of a tank. Then, the tank was filled with water and the height of the water was kept constant while the water was flowing through the scaffold under gravity and there was no water leakage from the scaffold/tank interface. The volume of water passing through the scaffold in 30 s was measured and this experiment was repeated for various fluid levels including 15, 25, 35, and 45 mm for all the scaffolds. The longitudinal permeability of scaffolds was calculated by Darcy's equation (Equation (3)):

$$k = -\frac{\mu \, \mathrm{q}}{A \frac{\Delta p}{l}} \quad (3)$$

where q is the fluid flow rate measured for each scaffold, μ is the fluid viscosity, A and l represent the cross-sectional area and length of scaffolds, respectively, and Δp is the hydrostatic pressure ($\Delta p = \rho g h$, where ρ, g, and h indicate fluid density, acceleration of gravity, and height of the fluid, respectively).[35]

Numerical analysis of fluid flow:

Numerical analysis of permeability was performed *via* computational fluid dynamics (CFD) procedures using Abaqus software to simulate fluid flow in the scaffolds. The cross-sectional binary images of scaffold models (fluid phase) were used to generate voxel-based 3D mesh models *via* a MATLAB code. The models were represented with an element size

of 0.13 mm resulting in the total mesh number of ~500,000-1,500,000 based on the previous mesh convergence studies.[36] Boundary conditions of zero pressure at the outlet and initial velocity of 10^{-4} m/s were defined at the inlet. A no-slip boundary condition was also set at the solid-fluid interface. Water with a density of 1000 kg/m^3 and viscosity of 0.001 Pa·s was specified as a working fluid. The Navier-Stokes and continuity equations were solved, and average pressure obtained for the nodes at the inlet was calculated to obtain computational permeability according to Equation (3).

Live/dead assay:

Mouse fibroblast 3T3 cells were cultured in 175 cm^2 cell culture flasks using 25 ml DMEM mixed with 1 %w/v streptomycin-penicillin and 10 %w/v fetal bovine serum (FBS).[37] To perform 3D cell culture, gelatin templates (designed with P-surface at 0.42 RD) were prepared and sterilized under UV for 30 min. Then, 10 %w/v GelMA was mixed with photoinitiator (as described in section 0) and the pH of the solution was adjusted by adding HCl to be fixed at ~7. Then, 3T3 cells were suspended in the GelMA solution (at ~1×10^7 cells/ml cell density). The gelatin template was placed in a 12-well plate. Then, 1.25 ml of cell-encapsulated GelMA was cast into the gelatin template and crosslinked. The porous GelMA scaffold was obtained after dissolving the gelatin template in media during incubation at 37 °C. Bulk solid cell-encapsulated GelMA (thickness of ~1 mm) samples were prepared as a control. The live/dead assay (Biotium) was conducted to evaluate the cell viability of the cell-encapsulated scaffolds. The live/dead cell staining solution was prepared by mixing two fluorescent probes (12 μl ethidium homodimer-1 and 3 μl of calcein) in 6 mL DPBS. After washing the samples in DPBS, they were immersed in the staining solution and incubated for ~40 min. Then, the samples were washed by DPBS. Eventually, fluorescence imaging was performed (at days 1, 3, and 5) using an Axio Observer 5, Zeiss, Germany fluorescence microscope. Imaging was conducted at the excitation/emission wavelengths of 494/515 nm for calcein (green), and 528/617 nm for ethidium homodimer-1 (red). Finally, the cell viability of porous and bulk GelMA samples were calculated as the ratio of live cells to the total number of cells using FIJI image processing software.

In vivo biocompatibility study:

All the *in vivo* studies were conducted under an approved animal protocol by The UCLA Animal Research Committee (ARC#2017-096-01). Male rats provided by Charles River Laboratories (South San Francisco, USA), weighing ~250-300 g, were acclimatized before the experiments for a one-week period. The rats were maintained in the specific pathogen-free (SPF) facilities at 25 °C and fed with purified water and the standard laboratory pellets. All the surgical procedures were conducted under general anesthesia. To achieve analgesia, isoflurane (1.5 %v/v in O_2 gas) was used and carprofen was subcutaneously injected into the rats. The fabricated cylindrical GelMA scaffolds P structure at 0.58 and 0.42 RD (dimensions of ~20 mm diameter and ~10 mm height) were cut in ¼ circle with ~3.3 mm height (one unit cell layer) and subcutaneously implanted. The bulk GelMA hydrogel with similar dimensions was used as controls. The implantation was performed with a ~15 mm surgical incision after shaving the skin and sterilization (using 70 %v/v ethanol and 0.2 %w/v iodophor). The rats were then euthanized for two weeks under carbon dioxide inhalation. The scaffolds and the adjacent tissues were extracted and treated with 10 %v/v

formalin, followed by hematoxylin and eosin (H&E) staining to analyze the state of cell growth around the samples.

Statistical analyses:

The experimental measurements were measured in at least triplicate, unless otherwise noted. The reported values represent mean ± standard deviation. Statistical analyses were performed using one-way analysis of variance (ANOVA) in GraphPad Prism 8.0 where the P values of smaller than 0.05 was considered statistically significant.

Supplementary Material

Refer to Web version on PubMed Central for supplementary material.

Acknowledgements

We acknowledge financial support from the National Institutes of Health (1R01AR073135-01A1). The funding from The Natural Sciences and Engineering Research Council of Canada (NSERC) Network for Holistic Innovation in Additive Manufacturing (HI-AM) is appreciated. The authors thank the staff of the Molecular Instrumentation Center in the UCLA Department of Chemistry for help with GCMS instrument operation. The assistance of Dr. Han-Jun Kim in animal studies is also appreciated.

References

[1]. Himmels P, Paredes I, Adler H, Karakatsani A, Luck R, Marti HH, Ermakova O, Rempel E, Stoeckli ET, Ruiz de Almodóvar C, Nat. Commun 2017, 8, 14583. [PubMed: 28262664]

[2]. a)Kolesky DB, Homan KA, Skylar-Scott MA, Lewis JA, Proc. Natl. Acad. Sci. U.S.A 2016, 113, 3179; [PubMed: 26951646] b)Miller JS, Stevens KR, Yang MT, Baker BM, Nguyen D-HT, Cohen DM, Toro E, Chen AA, Galie PA, Yu X, Chaturvedi R, Bhatia SN, Chen CS, Nat. Mater 2012, 11, 768; [PubMed: 22751181] c)Kolesky DB, Truby RL, Gladman AS, Busbee TA, Homan KA, Lewis JA, Adv. Mater 2014, 26, 3124. [PubMed: 24550124]

[3]. a)Tang Y, Lin S, Yin S, Jiang F, Zhou M, Yang G, Sun N, Zhang W, Jiang X, Biomaterials 2020, 232, 119727; [PubMed: 31918223] b)De France KJ, Xu F, Hoare T, Adv. Healthcare Mater 2018, 7, 1700927.

[4]. Grenier J, Duval H, Barou F, Lv P, David B, Letourneur D, Acta Biomater. 2019, 94, 195. [PubMed: 31154055]

[5]. a)Rusakov D, Menner A, Bismarck A, Macromol. Rapid Commun 2020, 41, 2000110;b)Prasad A, Sankar MR, Katiyar V, Mater. Today: Proc 2017, 4, 898.

[6]. a)Hossain Rakin R, Kumar H, Rajeev A, Natale G, Menard F, Li ITS, Kim K, Biofabrication 2021, 13, 044109;b)Ambhorkar P, Rakin RH, Wang Z, Kumar H, Kim K, Addit. Manuf 2020, 36, 101459.

[7]. a)Davoodi E, Sarikhani E, Montazerian H, Ahadian S, Costantini M, Swieszkowski W, Willerth SM, Walus K, Mofidfar M, Toyserkani E, Khademhosseini A, Ashammakhi N, Adv. Mater. Technol 2020, 5, 1901044; [PubMed: 33072855] b)Zhang H, Cong Y, Osi AR, Zhou Y, Huang F, Zaccaria RP, Chen J, Wang R, Fu J, Adv. Funct. Mater 2020, 30, 1910573;c)Johnston TG, Yuan S-F, Wagner JM, Yi X, Saha A, Smith P, Nelson A, Alper HS, Nat. Commun 2020, 11, 563; [PubMed: 32019917] d)Xie R, Zheng W, Guan L, Ai Y, Liang Q, Small 2020, 16, 1902838.

[8]. a)Cheng C, Moon YJ, Kim SH, Jeong Y-C, Hwang JY, Chiu GTC, Han B, Int. J. Heat Mass Transfer 2020, 150, 119327;b)Davoodi E, Fayazfar H, Liravi F, Jabari E, Toyserkani E, Addit. Manuf 2020, 32, 101016;c)Jabari E, Liravi F, Davoodi E, Lin L, Toyserkani E, Addit. Manuf 2020, 35, 101330.

[9]. a)Hong H, Seo YB, Kim DY, Lee JS, Lee YJ, Lee H, Ajiteru O, Sultan MT, Lee OJ, Kim SH, Park CH, Biomaterials 2020, 232, 119679; [PubMed: 31865191] b)Teng C-L, Chen J-Y, Chang

T-L, Hsiao S-K, Hsieh Y-K, Villalobos Gorday K, Cheng Y-L, Wang J, Biofabrication 2020, 12, 035024. [PubMed: 31918413]

[10]. Mishra AK, Wallin TJ, Pan W, Xu P, Wang K, Giannelis EP, Mazzolai B, Shepherd RF, Sci. Rob 2020, 5, eaaz3918.

[11]. a)Ali MA, Rajabi M, Sudhir Sali S, Curr. Opin. Chem. Eng 2020, 28, 127;b)Unagolla JM, Jayasuriya AC, Appl. Mater. Today 2020, 18, 100479; [PubMed: 32775607] c)Hu Y, Da L, Zhang W, Yang C, Wu Y, Dong G, presented at Proceedings of the Seventh Asia International Symposium on Mechatronics, Singapore 2020.

[12]. Chimene D, Kaunas R, Gaharwar AK, Adv. Mater 2020, 32, 1902026.

[13]. Yamaguchi S, Ueno A, Akiyama Y, Morishima K, Biofabrication 2012, 4, 045005. [PubMed: 23075800]

[14]. Chahal D, Ahmadi A, Cheung KC, Biotechnol. Bioeng 2012, 109, 2932. [PubMed: 22627805]

[15]. a)Zhou K, Dey M, Ayan B, Zhang Z, Ozbolat V, Kim MH, Khristov V, Ozbolat IT, Biomed. Mater 2021, 16, 045005;b)Ozbolat V, Dey M, Ayan B, Ozbolat IT, Biofabrication 2019, 11, 034101. [PubMed: 30884470]

[16]. Kinstlinger IS, Saxton SH, Calderon GA, Ruiz KV, Yalacki DR, Deme PR, Rosenkrantz JE, Louis-Rosenberg JD, Johansson F, Janson KD, Sazer DW, Panchavati SS, Bissig K-D, Stevens KR, Miller JS, Nat. Biomed. Eng 2020, 4, 916. [PubMed: 32601395]

[17]. a)Golden AP, Tien J, Lab Chip 2007, 7, 720; [PubMed: 17538713] b)Skylar-Scott MA, Uzel SGM, Nam LL, Ahrens JH, Truby RL, Damaraju S, Lewis JA, Sci. Adv 2019, 5, eaaw2459. [PubMed: 31523707]

[18]. a)Homan KA, Kolesky DB, Skylar-Scott MA, Herrmann J, Obuobi H, Moisan A, Lewis JA, Sci. Rep 2016, 6, 34845; [PubMed: 27725720] b)Wu W, DeConinck A, Lewis JA, Adv. Mater 2011, 23, H178; [PubMed: 21438034] c)Song KH, Highley CB, Rouff A, Burdick JA, Adv. Funct. Mater 2018, 28, 1801331.

[19]. Tocchio A, Tamplenizza M, Martello F, Gerges I, Rossi E, Argentiere S, Rodighiero S, Zhao W, Milani P, Lenardi C, Biomaterials 2015, 45, 124. [PubMed: 25662502]

[20]. a)Contessi Negrini N, Bonnetier M, Giatsidis G, Orgill DP, Farè S, Marelli B, Acta Biomater. 2019, 87, 61; [PubMed: 30654214] b)Wang M, Yang X, Liang L, Chem J. 2020, 2020, 3148652.

[21]. Gelber MK, Hurst G, Comi TJ, Bhargava R, Addit. Manuf 2018, 22, 38.

[22]. a)Davoodi E, Montazerian H, Haghniaz R, Rashidi A, Ahadian S, Sheikhi A, Chen J, Khademhosseini A, Milani AS, Hoorfar M, Toyserkani E, ACS Nano 2020, 14, 1520; [PubMed: 31904931] b)Szklanny AA, Machour M, Redenski I, Chochola V, Goldfracht I, Kaplan B, Epshtein M, Simaan Yameen H, Merdler U, Feinberg A, Seliktar D, Korin N, Jaroš J, Levenberg S, Adv. Mater 2021, 2102661.

[23]. Pimienta V, Brost M, Kovalchuk N, Bresch S, Steinbock O, Angew. Chem. Int. Ed 2011, 50, 10728.

[24]. Davoodi E, Montazerian H, Esmaeilizadeh R, Darabi AC, Rashidi A, Kadkhodapour J, Jahed H, Hoorfar M, Milani AS, Weiss PS, Khademhosseini A, Toyserkani E, ACS Appl. Mater. Interfaces 2021, 13, 22110. [PubMed: 33945249]

[25]. Noshadi I, Hong S, Sullivan KE, Shirzaei Sani E, Portillo-Lara R, Tamayol A, Shin SR, Gao AE, Stoppel WL, Black Iii LD, Khademhosseini A, Annabi N, Biomater. Sci 2017, 5, 2093. [PubMed: 28805830]

[26]. a)Lee A, Hudson A, Shiwarski D, Tashman J, Hinton T, Yerneni S, Bliley J, Campbell P, Feinberg A, Science 2019, 365, 482; [PubMed: 31371612] b)Erdem A, Darabi MA, Nasiri R, Sangabathuni S, Ertas YN, Alem H, Hosseini V, Shamloo A, Nasr AS, Ahadian S, Adv. Healthcare Mater 2020, 9, 1901794.

[27]. Ashammakhi N, Ahadian S, Xu C, Montazerian H, Ko H, Nasiri R, Barros N, Khademhosseini A, Mater. Today Bio 2019, 1, 100008.

[28]. Wisotzki EI, Hennes M, Schuldt C, Engert F, Knolle W, Decker U, Käs JA, Zink M, Mayr SG, J. Mater. Chem. B 2014, 2, 4297. [PubMed: 32261568]

[29]. Zhang Q, Jiang Y, Zhang Y, Ye Z, Tan W, Lang M, Polym. Degrad. Stab 2013, 98, 209.

[30]. Montazerian H, Mohamed MGA, Montazeri MM, Kheiri S, Milani AS, Kim K, Hoorfar M, Acta Biomater. 2019, 96, 149. [PubMed: 31252172]

[31]. Budday S, Ovaert TC, Holzapfel GA, Steinmann P, Kuhl E, Arch. Comput. Methods Eng 2019, 1.

[32]. Montazerian H, Zhianmanesh M, Davoodi E, Milani AS, Hoorfar M, Mater. Des 2017, 122, 146.

[33]. Lu Y, Cheng L, Yang Z, Li J, Zhu H, PLoS One 2020, 15, e0238471. [PubMed: 32870933]

[34]. Nichol JW, Koshy ST, Bae H, Hwang CM, Yamanlar S, Khademhosseini A, Biomaterials 2010, 31, 5536. [PubMed: 20417964]

[35]. Rahbari A, Montazerian H, Davoodi E, Homayoonfar S, Comput. Methods Biomech. Biomed. Eng 2017, 20, 231.

[36]. Montazerian H, Davoodi E, Asadi-Eydivand M, Kadkhodapour J, Solati-Hashjin M, Mater. Des 2017, 126, 98.

[37]. Vinci VA, Parekh SR, Handbook of Industrial Cell Culture: Mammalian, Microbial, and Plant Cells, Springer Science & Business Media, 2002.

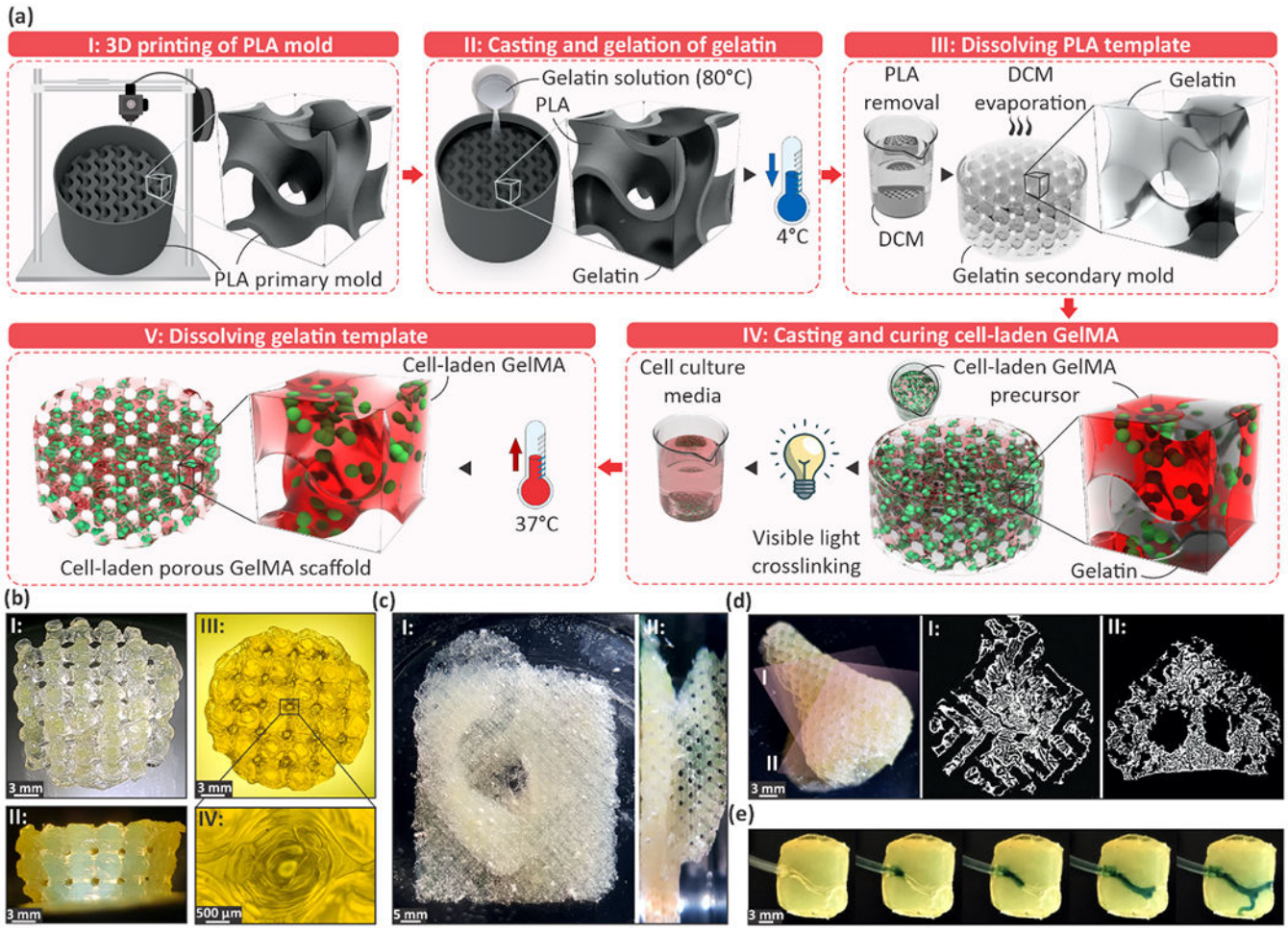

Figure 1. The three-dimensional (3D) bio-templating scheme for fabrication of thick 3D structured cell-laden gelatin methacryloyl (GelMA) constructs with patterned tortuous macro-channels.

(a) Schematic illustration of the proposed fabrication procedure. I: 3D printing of the primary templates using extrusion methods based on FDM, II: casting gelatin at high temperature (80 °C) in the PLA templates followed by physical gelation of gelatin at the low temperature (4 °C). III: Development of the porous gelatin template by the dissolution of PLA plastic in dichloromethane (DCM), and DCM removal in water for ~1 day. IV: Casting a cell-laden GelMA prepolymer solution *via* a visible light crosslinking procedure. V: removing the gelatin template from a network of photo-crosslinked cell-encapsulated GelMA hydrogel at the incubation temperature during the cell culture (37 °C). (b) Images from different views of the fabricated GelMA hydrogel constructs. I: Top-side view of hydrogel with the P structure at 0.42 relative density (RD). II, III: Side and top views of the scaffold with 0.70 RD, respectively. IV: Magnified image of the micro-scale pores in the fabricated scaffolds. Demonstration of complex 3D human tissue models, *i.e.*, (c) ear I: top view, II: side view, and (d) nose fabricated using the proposed procedure (I, II: micro-computed tomography (μ-CT) images of the freeze-dried porous nose models at cross-sections shown in (d)). (e) Demonstration of open channels fabricated inside a GelMA hydrogel (resembling complex-shaped blood vessels).

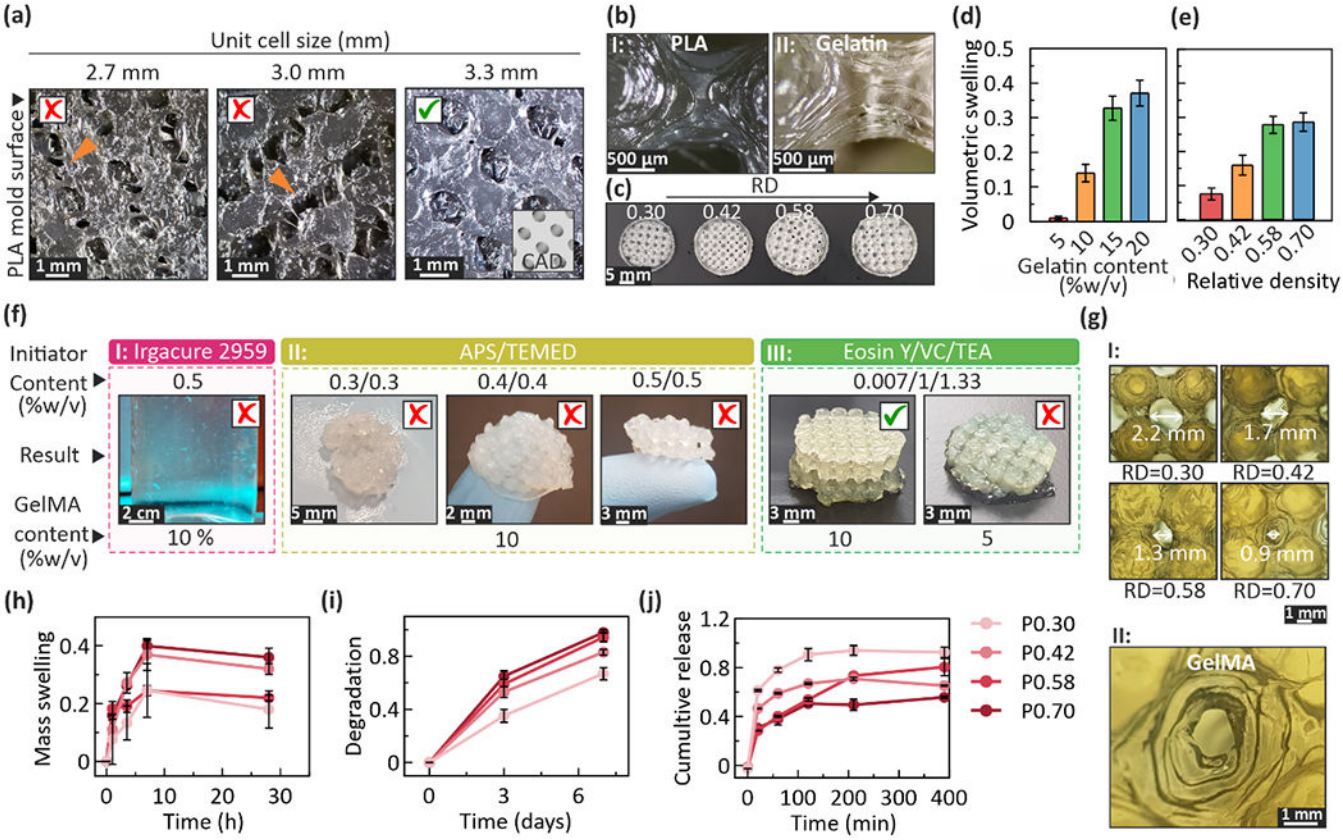

Figure 2. Optimization of the fabrication process and physical properties of the gelatin methacryloyl (GelMA) scaffold constructs.

(a) Printability evaluation of poly(lactic acid) (PLA) at different unit cell size scales of 2.7 mm, 3.0 mm, and 3.3 mm. Arrows show the defects in the 3D printed constructs. Minimum feature sizes were maintained at 3.3 mm unit cell sizes and above. (b) Microscope images of the scaffold structure and surface stain step patterns for I: PLA templates and II: 10 %w/v gelatin templates. (c) Optical image of the swelling behavior of gelatin templates at different gelatin relative density (RD) values. Characterization of volumetric swelling of gelatin templates as a function of (d) gelatin concentration and (e) the gelatin scaffold RD. The data represent means and standard deviations (n=3). (f) Polymerization behavior of GelMA using different initiator systems I: Irgacure 2959, II: ammonium persulfate (APS)/*N,N,N,N*-tetramethylethylenediamine (TEMED), and III: EosinY/*N*-vinylcaprolactams (VC)/triethanolamine (TEA) to form crosslinked GelMA structures at 10 %w/v GelMA concentration. (g) I: Microscopic images of the pore topology and size for the GelMA scaffolds with P structure at different RD values. II: Stair-step GelMA surface topology transferred from gelatin molds. Characterization of (h) mass swelling ratio, (i) degradation, and (j) cumulative release of Rhodamine B over time from scaffolds with P structure at different RD values. The data represent means and standard deviations (n=3).

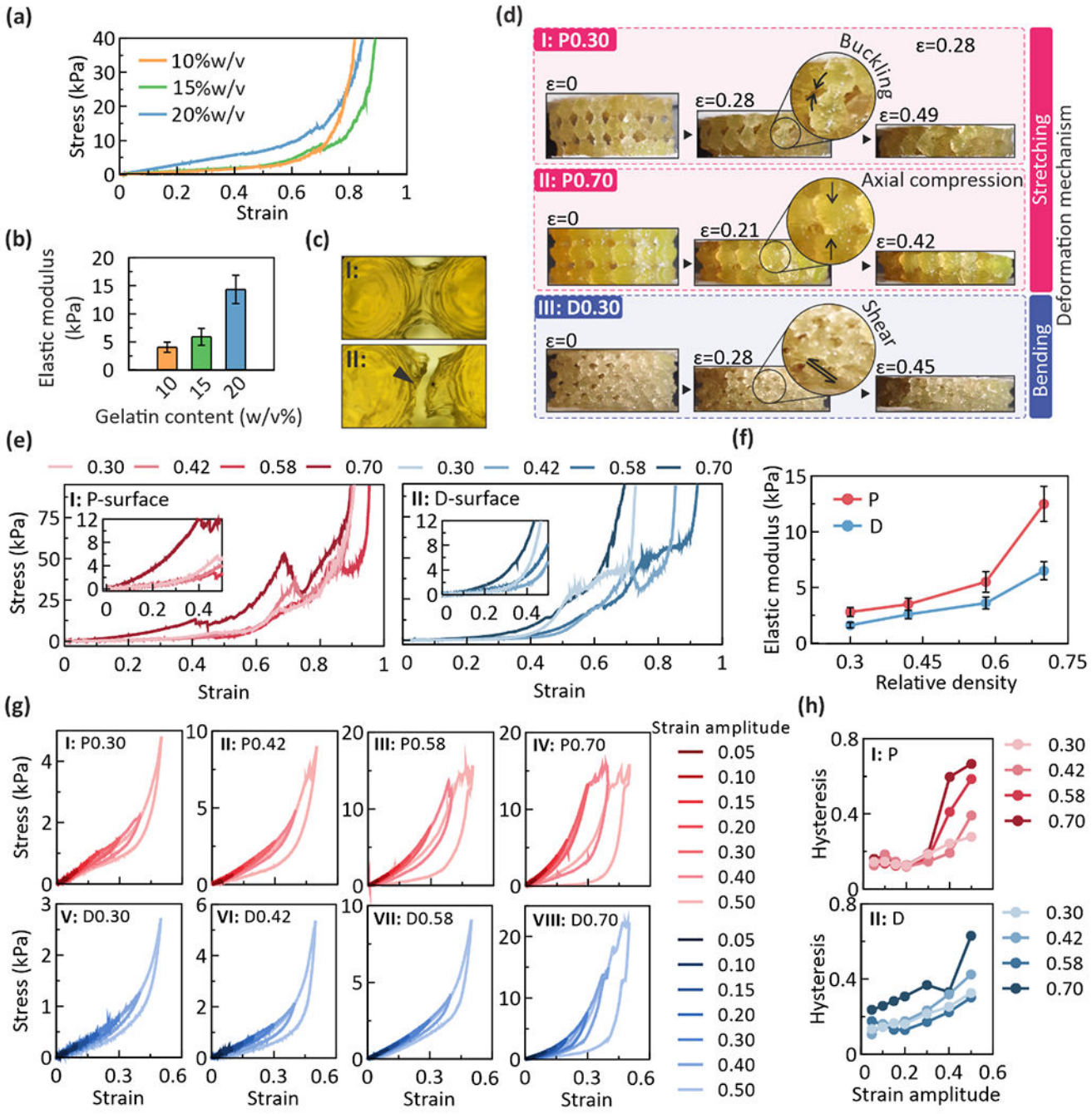

Figure 3. Mechanical characterization of porous gelatin methacryloyl (GelMA) constructs.

(a) The effect of GelMA concentration on the stress-strain curves for P structure at 0.42 relative density (RD), and (b) variation of compressive elastic modulus with GelMA concentration. The data represent means and standard deviations (n=3). (c) Optical images representative of brittle failure of linkages in P structure scaffold under compressive deformation. Representation of the linkage I: before and II: after failure. (d) The deformation mechanisms of GelMA scaffolds for P structure at I: 0.30 and II: 0.70 and III: D structure at 0.30 RD for different strain values (ε). (e) The stress-strain curves corresponding

to the cyclic load for I: P and II: D structures at different RD values, and (f) elastic modulus-RD relationships for P and D structures. The data represent means and standard deviations (n=3). (g) The cyclic stress-strain curves with increasing strain amplitude for P structure at I: 0.30, II: 0.42, III: 0.58, IV: 0.70, and D structure at V: 0.30, VI: 0.42, VII: 0.58, and VIII: 0.70 RD values. (h) The results of hysteresis *versus* the strain amplitude for I: P and II: D structures.

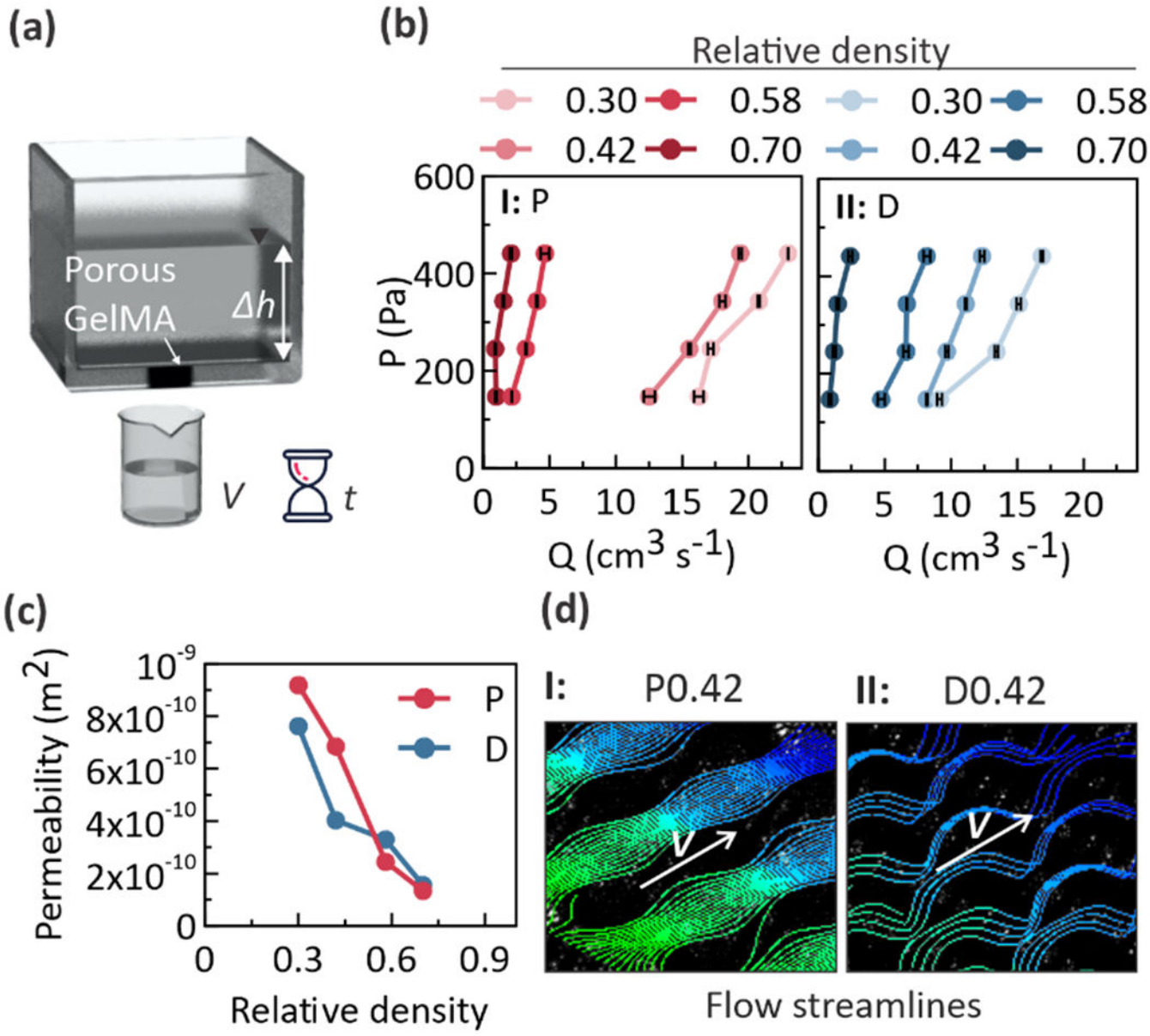

Figure 4. Fluid flow permeability of porous gelatin methacryloyl (GelMA) scaffolds.

(a) Schematic representation of the constant head permeability test setup. (b) Variations of pressure drop (P) with fluid flow rate (Q) for GelMA scaffolds designed with I: P-surface and II: D-surface pore shapes. The data represent means and standard deviations (n=3). (c) Permeability analysis of GelMA scaffolds as a function of pore shape and relative density (RD). (d) The results of computational flow streamlines obtained from the computational fluid dynamics (CFD) analysis of fluid flow in I: P and II: D structure at 0.42 RD.

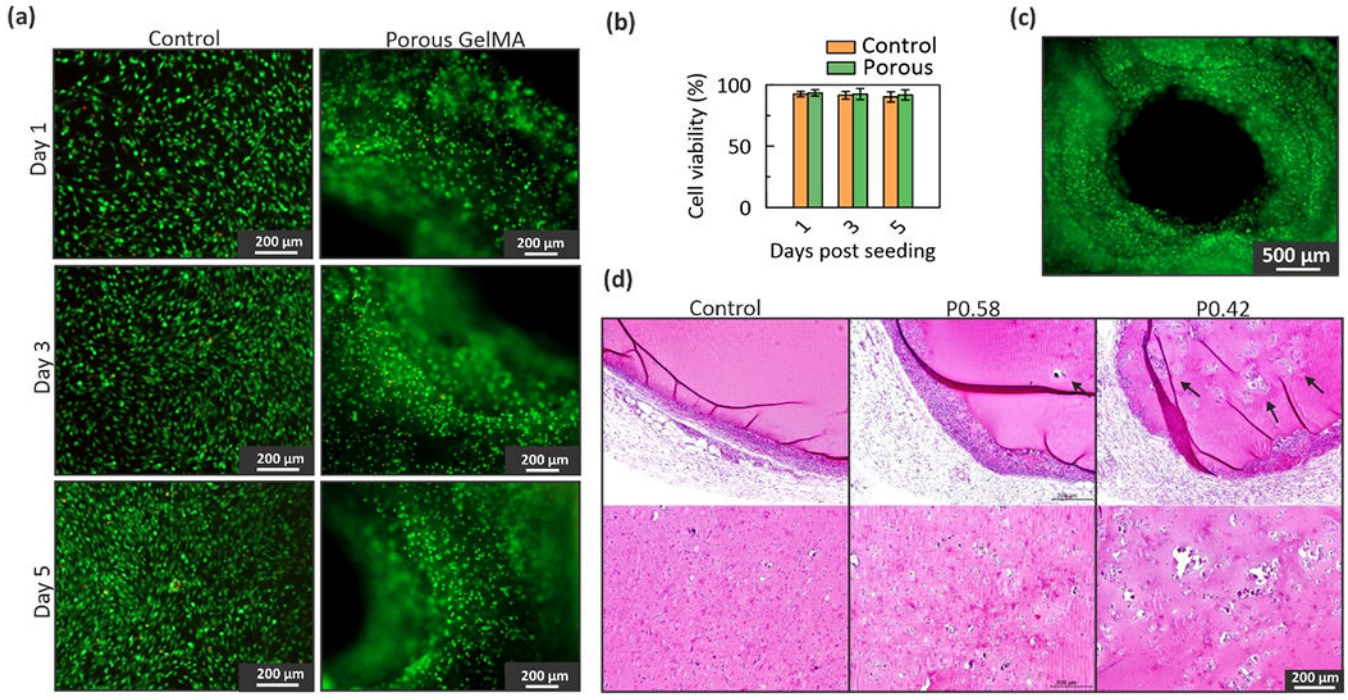

Figure 5. *In vitro* and *in vivo* biocompatibility analysis of porous gelatin methacryloyl (GelMA) scaffolds.

(a) Live/dead fluorescent images of cell-laden control and porous bulk GelMA scaffold (green: live and red: dead cells). (b) Cell viability of cell-laden control and porous scaffold on days 1, 3, and 5 following cell encapsulation. The data represent means and standard deviations (n=3). (c) The interconnected pores in the GelMA scaffolds maintained high cell viability in thick scaffolds. (d) The hematoxylin and eosin (H&E) staining of the *in vivo* implanted scaffolds with different relative densities (RD) of 0.42 and 0.58 as well as bulk GelMA after two weeks. Low RD scaffolds (associated with higher permeability and pore size) facilitated cell growth inside the hydrogel structure.